water

MDPI

Article

ZnO-CuO Nanocomposite as an Efficient Adsorbent for As(III) Removal from Water

Jesús Plácido Medina Salas [1,*], Francisco Gamarra Gómez [1], Elisban Juani Sacari Sacari [1,2,*], Wilson Orlando Lanchipa Ramos [1], Rocío María Tamayo Calderón [3], Efracio Mamani Flores [4], Víctor Yapuchura Platero [5], Walter Dimas Florez Ponce de León [6] and Elmer Marcial Limache Sandoval [7]

[1] Laboratorio de Nanotecnología (NanoLab), Facultad de Ingeniería, Universidad Nacional Jorge Basadre Grohmann, Av. Miraflores s/n, Tacna 23003, Peru; fgamarrag@unjbg.edu.pe (F.G.G.)
[2] Centro de Energías Renovables de Tacna (CERT), Facultad de Ciencias, Universidad Nacional Jorge Basadre Grohmann, Av. Miraflores s/n, Tacna 23003, Peru
[3] Centro de Microscopia Electrónica, Facultad de Ingeniería de Procesos, Universidad Nacional de San Agustín, Arequipa 04001, Peru
[4] Departamento de Física Aplicada, Facultad de Ciencias, Universidad Nacional Jorge Basadre Grohmann, Av. Miraflores s/n, Tacna 23003, Peru
[5] Departamento de Ingeniería Civil, Facultad de Ingeniería Civil, Arquitectura y Geotecnia, Universidad Nacional Jorge Basadre Grohmann, Av. Miraflores s/n, Tacna 23003, Peru
[6] Departamento de Química, Facultad de Ingeniería, Universidad Nacional Jorge Basadre Grohmann, Av. Miraflores s/n, Tacna 23003, Peru
[7] Grupo de Investigación HIDROCIENCIA, Facultad de Ciencias de la Salud, Universidad Privada de Tacna, Av. Jorge Basadre Grohmann s/n, Pocollay, Tacna 23000, Peru
* Correspondence: jmedinas@unjbg.edu.pe (J.P.M.S.); esacaris@unjbg.edu.pe (E.J.S.S.)

Abstract: Arsenic (III) exposure, often from contaminated water, can have severe health repercussions. Chronic exposure to this toxic compound is linked to increased risks of various health issues. Various technologies exist for arsenic (III) removal from contaminated water sources. This work synthesized ZnO-CuO nanocomposites through ultrasound-assisted coprecipitation, generating abundant hydroxylated sites via the deposition of ZnO nanoparticles onto CuO sheets for enhanced arsenic (III) adsorption. Structural characterization verified the formation of phase-pure heterostructures with emergent properties. Batch studies demonstrated exceptional 85.63% As(III) removal at pH 5, where binding with prevalent neutral H_3AsO_3 occurred through inner-sphere complexation with protonated groups. However, competing anions decreased removal through site blocking. Favorable pseudo-second order chemisorption kinetics and the 64.77 mg/g maximum Langmuir capacity revealed rapid multilayer uptake, enabled by intrinsic synergies upon nanoscale mixing of Zn/Cu oxides. The straightforward, energy-efficient ultrasonic production route makes this material promising for real-world water treatment integration.

Keywords: nanocomposite; ZnO-CuO; arsenic; water treatment; ultrasonication; chemisorption

Citation: Medina Salas, J.P.; Gamarra Gómez, F.; Sacari Sacari, E.J.; Lanchipa Ramos, W.O.; Tamayo Calderón, R.M.; Mamani Flores, E.; Yapuchura Platero, V.; Florez Ponce de León, W.D.; Sandoval, E.M.L. ZnO-CuO Nanocomposite as an Efficient Adsorbent for As(III) Removal from Water. *Water* **2023**, *15*, 4318. https://doi.org/10.3390/w15244318

Academic Editors: Shakeel Ahmad, Shicheng Zhang, Mujtaba Baqar and Eric Danso-Boateng

Received: 18 September 2023
Revised: 12 December 2023
Accepted: 14 December 2023
Published: 18 December 2023

1. Introduction

Contamination of water by toxic heavy metals is a major issue that has serious consequences for human health and the natural environment [1]. While heavy metals occur naturally, human activities like mining, industrial processes, and agricultural runoff contribute to their release into the environment [2]. Consequently, heavy metals accumulate in water, soil, and air, posing a threat to plants, animals, and humans [3].

One such heavy metal is arsenic, which exists naturally but is also discharged into the environment through human practices like mining, smelting, and coal burning [4,5].

High arsenic levels have been reported in groundwater and tap water in regions of Asia, including Bangladesh, India, and China [6,7]. Alarming concentrations are also prevalent in some Latin American countries, such as Argentina [8], Chile [9], Mexico [10],

and Peru [11,12]. In Peru specifically, arsenic contamination is linked to mining activities and the abundance of volcanic systems with high arsenic content [12,13]. The city of Tacna, located in southern Peru, has reported arsenic concentrations of up to 0.5 mg/L in drinking water from reservoirs recharged by arsenic-rich volcanic rocks [14]. This level far exceeds the 10 µg/L limit recommended by the World Health Organization [15].

Arsenic contamination of water sources presents serious health risks to humans. Exposure to arsenic can result in various health problems [16], including skin lesions [17], gastrointestinal and neurological issues [18,19], cancer [20,21], as well as birth defects and developmental challenges in children [22].

Arsenic (III) is the predominant form of arsenic in water and is notably toxic compared to other forms [23], making its removal challenging. Arsenic (III) acts as a reducing agent and can chemically transform when exposed to oxygen, resulting in its conversion to arsenic (V), which exhibits reduced toxicity and improved water removal capabilities [24].

A broad spectrum of techniques and technologies can be utilized for arsenic removal from water, but their efficacy varies based on factors such as arsenic type, concentration, and cost [25]. Common technologies include precipitation, coagulation, adsorption, and ion exchange [26]. Precipitation employs chemicals to induce arsenic precipitation, while coagulation facilitates the clumping of arsenic particles for easier removal [27]. Adsorption employs materials to bind arsenic to their surfaces, and ion exchange uses resins to exchange arsenic ions for other ions [28].

Adsorption is the process by which a substance adheres to the surface of another substance and offers significant advantages over other technologies. It is highly efficient, cost-effective, versatile, and safe for arsenic removal from water [29]. For this purpose, different materials that could remove arsenic from water have been studied, such as TiO_2 [30] and their composites [31,32], iron-based materials [33,34], nickel-based materials [35], perovskite-type materials, such as $CaTiO_3$ [36], graphene-based materials [37], carbon nanotubes [38], and other materials [39]. In terms of effectiveness and cost, the adsorption method is the most efficient, but its operation is still expensive.

CuO, ZnO, and ZnO/CuO nanomaterials are promising adsorbents for arsenic remediation [40–43] on account of their substantial surface area and porous properties [44], hydroxyl functional groups on the surface [45], variable surface charges [46], redox activity [47], wide pH stability [48], reusability [49], low cost, and easy synthesis methods [50–56]. These properties facilitate arsenic adsorption through surface complexation, ion exchange, electrostatic interactions, coprecipitation, and redox reactions. However, the specific mechanisms of arsenite adsorption are not well understood and require further research to optimize nanosorbent design for efficient arsenic removal [57].

The main objectives of this research involved the synthesis of ZnO/CuO nanocomposite at different concentrations using an ultrasound-assisted precipitation method. Subsequently, the synthesized materials were subjected to comprehensive characterization to evaluate the impact of the composition on their structural, vibrational, and morphological properties, as well as their effectiveness in arsenic (III) removal. In this investigation, a comprehensive set of analytical methods was utilized. These techniques included X-ray diffraction (XRD), Fourier-transform infrared (FTIR) spectroscopy, scanning electron microscopy (SEM), and BET surface area. Furthermore, batch experiments to evaluate the arsenic adsorption capabilities of the synthesized materials were also performed.

2. Materials and Methods

2.1. Materials

All the chemicals employed in this investigation were of analytical quality and were utilized without any additional purification steps. 2-Propanol, Zinc (II) Acetate Dihydrate, Copper (II) Nitrate Trihydrate, Sodium Hydroxide, Hydrochloric Acid (37%), Sodium (meta) Arsenite, Sodium Chloride, Sodium Nitrate, and Sodium Sulfate were supplied by Merck Company (Darmstadt, Germany).

2.2. ZnO-CuO Nanocomposites Synthesis

The synthesis of the ZnO-CuO nanocomposite was achieved by employing the ultrasound-assisted precipitation method. For this purpose, five samples were synthesized with 00:100 (0: 3.9922 g), 25:75 (1.09745 g: 2.99475 g), 50:50 (2.195 g: 1.9965 g), 75:25 (3.2925 g: 0.99825 g), and 100:00 (4.3923 g: 0) molar ratios of zinc (II) acetate dihydrate and copper (II) nitrate trihydrate, respectively. Each of these reagents was mixed and dissolved by a 35 kHz ultrasound cleaner (VWR Symphony, Radnor, PA, USA) in 500 mL of 2-propanol for 30 min and labeled as an A solution. Similarly, 0.08 M (1.6 g) of sodium hydroxide was dissolved in 500 mL of ultrapure water for 30 min and labeled as a B solution. After 30 min of sonication, the B solution was added dropwise to the A solution and then kept in constant sonication for an additional 30 min. Subsequently, the resulting solid was subjected to several rounds of ultrapure water washing, followed by filtration, drying at room temperature, and finally, calcination at 400 °C for a period of 2 h. The obtained samples were labeled CuO, ZnO-CuO (25:75), ZnO-CuO (50:50), ZnO-CuO (75:25), and ZnO, according to the molar ratio.

2.3. Characterization

The X-ray diffraction (XRD) patterns of the ZnO-CuO nanocomposites were recorded using a diffractometer from AERIS Research (Malvern Panalytical Ltd., Almedo, The Netherlands) with Ni-filtered CuKα radiation (wavelength 1.5406 Å) over a 2θ range from 20° to 80°. The crystallite size and structural parameters were determined by Rietveld refinement using X'Pert HighScore Plus software version 4.9. Nitrogen adsorption analysis at 77 K was carried out on a Gemini VII surface area analyzer from Micromeritics Instrument Co. (Norcross, GA, USA) to measure the specific surface area (BET) of the nanocomposites after degassing the sample at 200 °C under helium flow for 2 h. Attenuated total reflectance Fourier-transform infrared (ATR-FTIR) spectroscopy over the 400–4000 cm^{-1} range was performed using a Bruker Invenio R spectrometer (Ettlingen, Germany) to acquire the vibrational spectra. A Thermo Scientific Quattro S field emission scanning electron microscope (FE-SEM) (Thermo Scientific Co., Eindhoven, The Netherlands) equipped with an UltraDry EDS detector was used to analyze the morphology of the samples and perform elemental analysis, and Thermo Scientific Talos F200i Transmission Electron Microscope (Thermo Scientific Co., Eindhoven, The Netherlands) was utilized to examine the shape and particle size of the samples. The arsenic (III) concentration was quantified using a flameless atomic absorption spectrometer (Shimadzu AA-6300, Shimadzu Scientific Instruments, Inc., Kyoto, Japan) with a graphite furnace atomizer (GFA-EX7i), employing a hollow cathode lamp (293.7 nm, 25 mA) for arsenic and a deuterium lamp for background correction.

2.4. Batch Adsorption Experiments

A 10 ppm arsenic (III) stock solution was prepared by dissolving 5.45 mg of sodium meta-arsenite ($NaAsO_2$) in 1 L of ultrapure water to provide the arsenic (III) adsorbate.

Batch adsorption experiments were then performed to evaluate the arsenic removal capacity of the synthesized ZnO-CuO nanocomposite materials. These batch tests served as a rapid screening tool for analyzing the adsorption capabilities of the nanocomposites by studying the depletion in arsenic(III) concentration when equilibrated with the nanocomposite adsorbent material under controlled conditions. In the experimental procedure, a solution consisting of 100 mL of water containing 10 ppm of arsenic (III) at pH 7 was subjected to a treatment involving the combination of 50 mg/L of adsorbent. The resultant solution was then stirred at a rate of 200 rpm for 2 h while maintaining a temperature of 25 degrees Celsius. The arsenic adsorption experiments were conducted in a darkened environment. Samples were collected at various time intervals; then, centrifugation was carried out at 6000 rpm for 5 min, and thereafter, the supernatant was analyzed utilizing graphite furnace atomic absorption spectroscopy.

2.5. Impact of pH on Arsenic Removal

To assess the impact of pH on the effectiveness of arsenic removal, a series of solutions was prepared. These solutions maintained a constant concentration of 10 ppm of arsenic (III) while varying the pH levels. The pH was changed by adding solutions of either sodium hydroxide or diluted hydrochloric acid. After an adsorption procedure that lasted for two hours, samples were collected, and subsequently, they were subjected to centrifugation at 6000 revolutions per minute. A graphite furnace atomic absorption spectrometer was used to analyze the supernatant.

The equilibrium adsorption isotherms of the sample with the better performance were studied by conducting batch experiments under dark conditions using 50 mg of the ZnO-CuO nanocomposite and varying initial arsenic (III) concentrations of 10, 20, 40, 60, 80, and 100 ppm dissolved in 100 mL of deionized water. The resultant adsorption data after 2 h of contact time were modeled using the linearized Langmuir and Freundlich isotherm equations.

The Langmuir model assumes monolayer coverage of energetically equivalent sites, while the Freundlich model accounts for multilayer adsorption on a heterogeneous surface. Analysis of the correlation coefficients and chi-square values from the linear regression fitting revealed that the Langmuir model better described the arsenic (III) adsorption behavior.

2.6. PZC of ZnO-CuO Nanocomposite

The point of zero charge (PZC) of ZnO-CuO nanocomposites with the most exceptional adsorption capabilities was determined using the salt addition method [58]. To elucidate, 40 mL of a 0.1 M $NaNO_3$ solution was aliquoted into nine separate Erlenmeyer flasks. The pH levels of the ZnO-CuO nanocomposite suspensions, spanning the range from 3 to 11, were adjusted by introducing either 0.1 M nitric acid or 0.1 M sodium hydroxide solutions, monitored with a pH meter (HI 5221, HANNA Instruments, Woonsocket, RI, USA). Following this, 0.02 g of ZnO-CuO nanocomposites were introduced into each flask and agitated at 150 rpm on an orbital shaker, maintaining a temperature of 30 °C for a duration of 24 h. Once equilibrium was reached, the contents were filtered, and the pH values of the filtrates were duly recorded. Subsequently, the PZC value, representing the pH at which the total surface charge on the adsorbent becomes neutral, was determined by plotting a graph correlating the initial pH with the change in pH.

2.7. Influence of Coexisting Ions on Arsenic Removal

To examine the effects of competing ions, test solutions were made using sodium salts of chloride, nitrate, and sulfate at varying concentrations of 100, 250, and 500 ppm.

The adsorption experiments were performed with an initial arsenic (III) concentration of 10 ppm and a dosage of 50 mg/L of adsorbent. A sodium hydroxide solution was employed to adjust the pH of the solutions to ~7.0.

After the batch adsorption tests were conducted for two hours, samples were collected from the test solutions containing the ZnO-CuO nanocomposite adsorbent and arsenic species. These samples were centrifuged at 4000 rpm for 5 min to separate out the adsorbent particles. Centrifugation facilitated the isolation of the supernatant from the solid adsorbent phase. The supernatant consisted of the residual arsenic species remaining in the solution after the adsorption process. This supernatant was then analyzed using a sensitive atomic absorption spectroscopy technique coupled with a graphite furnace atomizer.

3. Results and Discussion

3.1. X-ray Diffraction Results

X-ray diffraction (XRD) analysis provided critical insights into the crystalline phase composition, nanostructure, and structural parameters of the synthesized ZnO-CuO nanocomposites (Figure 1a). The samples contained two distinct components, hexagonal zincite ZnO (JCPDS 01-075-1526) and monoclinic tenorite CuO (JCPDS 00-005-0661), without

any additional impurity peaks. The relative intensity of the ZnO and CuO peaks varied proportionally with their composition ratios, as expected.

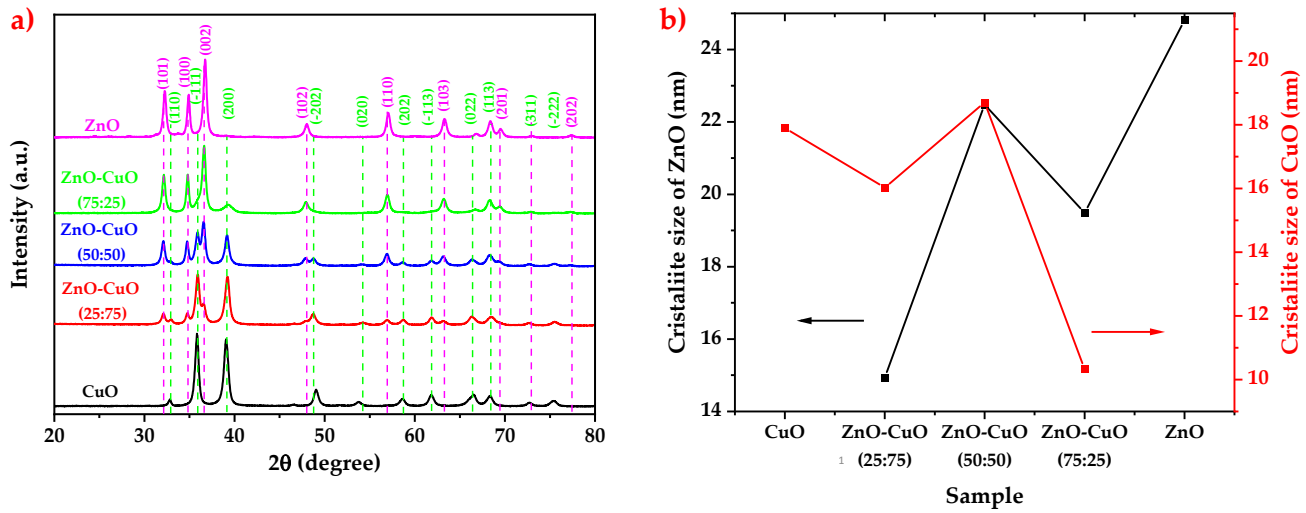

Figure 1. (**a**) X-ray diffraction profiles of ZnO-CuO nanocomposites and (**b**) Crystallite size of ZnO and CuO.

Detailed Rietveld refinement of the XRD patterns was performed using PANalytical HighScore Plus software V.4.9 to quantify the relative phase abundances, crystallite sizes, and lattice constants in the nanocomposites. The background was modeled using the Chebyshev function, and the pseudo-Voigt profile was applied for peak fitting. Table 1 summarizes the results of the nanocomposites.

Table 1. Structure-related parameters for ZnO-CuO nanocomposites.

Sample	CuO (100)	ZnO-CuO (25:75)		ZnO-CuO (50:50)		ZnO-CuO (75:25)		ZnO (100)
Phase	**CuO**	**ZnO**	**CuO**	**ZnO**	**CuO**	**ZnO**	**CuO**	**ZnO**
Crystal system	Monoclinic	Hexagonal	Monoclinic	Hexagonal	Monoclinic	Hexagonal	Monoclinic	Hexagonal
Phase percentage (%)	100	24.71	75.29	48.57	51.43	75.2	24.8	100
a (nm)	4.67793	3.25339	4.72394	3.25317	4.71857	3.25237	4.76458	3.24885
b (nm)	3.42191	3.25339	3.40375	3.25317	3.40595	3.25237	3.3736	3.24885
c (nm)	5.12759	5.21114	5.1312	5.21158	5.13222	5.21043	5.1187	5.20628
α (°)	90	90	90	90	90	90	90	90
β (°)	99.49249	90	99.95483	90	99.88692	90	99.96167	90
γ (°)	90	120	90	120	90	120	90	120
ρ (g/cm^3)	6.5	5.66	6.5	5.66	6.5	5.66	6.52	5.67
D (nm)	17.9	14.93	16.03	22.48	18.7	19.49	10.33	24.81
R_{exp} (%)	1.37993	1.32982		1.31176		1.32851		1.24266
R_{wp} (%)	2.23386	2.26934		2.24639		2.5136		2.16768
R_p (%)	1.74381	1.86191		1.96468		1.7781		1.58302
GOF	1.29957	1.31047		1.34613		1.25582		1.74439
SSA_{BET} (m^2/g)	22.3098 ± 0.0625 m^2/g	21.8229 ± 0.0198 m^2/g		17.7192 ± 0.2239 m^2/g		19.5901 ± 0.1120 m^2/g		18.4638 ± 0.0642 m^2/g

Excellent fitting confirmed that the samples contained highly crystalline zincite ZnO and tenorite CuO as the only phases with tunable relative compositions, as expected from the synthesis ratios. The ZnO crystallite size exhibited an initial increase from 14.93 nm to 22.48 nm as CuO content increased to 50%, which was attributed to CuO-mediated

nucleation and growth. However, at 75% CuO, the size reduced to 10.33 nm, indicating dominant ZnO growth inhibition effects, as depicted in Figure 1b and outlined in Table 1. These trends imply that complex synergistic interactions between ZnO and CuO modulate crystallite growth during nanocomposite formation. Furthermore, the specific surface area understandably correlated inversely with crystallite size, as displayed in Table 1.

3.2. FTIR Spectral Analysis

Fourier-transform infrared spectroscopy was employed for the detailed characterization of the chemical environments and bonding structures in the synthesized ZnO-CuO nanocomposites (Figure 2). The FTIR spectra provided complementary evidence, alongside XRD and microscopy, on the successful formation of ZnO and CuO phases with tunable compositions.

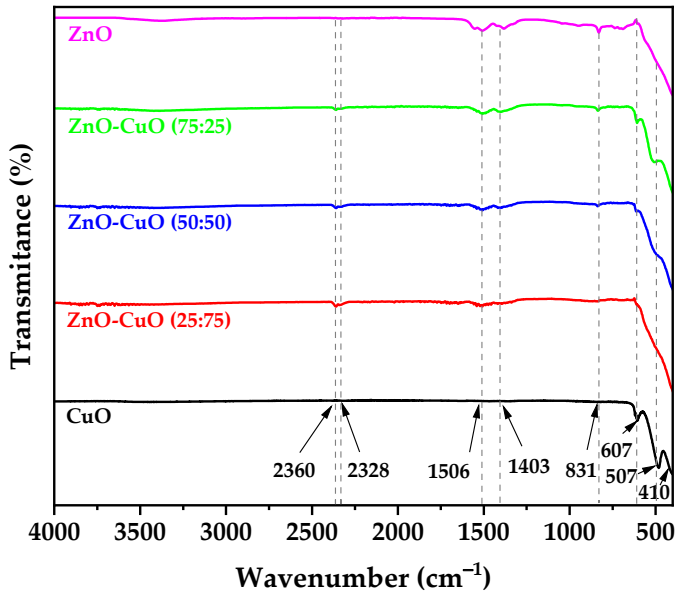

Figure 2. FTIR spectrums of ZnO-CuO nanocomposites.

The Zn-O and Cu-O metal–oxygen vibrational stretches confirmed the incorporation of ZnO and CuO, with relative intensities varying proportionally to the Zn and Cu content, as expected from the synthesis ratios. Specifically, the Zn-O peaks at 410 cm^{-1} and 607 cm^{-1} corresponded to the hexagonal wurtzite structure of the ZnO [59,60]. The Cu-O stretch at 507 cm^{-1} indicated the presence of a monoclinic CuO [61].

The FTIR spectra also exhibited small peaks at 2328 cm^{-1} and 2360 cm^{-1}, corresponding to the stretching vibrations of residual carboxyl groups. These leftover organic carboxyl moieties likely originated from the incomplete decomposition of the zinc acetate and 2-propanol precursors during the thermal treatment [62].

Additional signals observed at 1403 cm^{-1} and 1506 cm^{-1} were assigned to the symmetric stretching vibrations of carboxylate functionalities (COO^{-}) associated with residual acetate groups [63]. The relative intensities of the carboxyl and carboxylate peaks showed a direct correlation with the ZnO:CuO composition ratios. The higher the copper content, the greater the intensity of these peaks was observed. This variational trend aligns with the greater stability of copper acetate complexes compared to zinc acetates, leading to higher residuals at higher CuO contents.

The presence of residual organic groups like carboxylates and hydroxides revealed incomplete decomposition of the zinc acetate and 2-propanol precursors during the low-temperature ultrasonication treatment. This was likely responsible for the residual carbon observed in the EDS analysis (Table 2).

3.3. Scanning and Transmission Electron Microscopy

Field scanning electron microscopy (FE-SEM) and energy-dispersive X-ray spectroscopy (EDS) were applied to investigate both the morphology and elemental composition of ZnO-CuO composites. Figure 3 shows that the ZnO-CuO composites consist of CuO leaves covered by irregularly shaped ZnO nanoparticles (Figure 3). The increase in ZnO content tends to cover the CuO leaves progressively, as can be observed in Figure 3d,f,h), where CuO leaves were widely covered. EDS analysis was effectively utilized to validate and quantify the elemental composition. This technique allowed for the precise determination of the elemental ratios in ZnO-CuO composite materials. Table 2 reveals the relative abundance of Zn and Cu in the samples based on the elemental composition determined from the samples. Notably, the Zn/Cu ratio determined by EDS analysis closely matched both the anticipated values based on the molar composition used in the synthesis and the XRD results. This indicates that ZnO and CuO have been extensively incorporated, and the composites are homogeneous. Carbon content in samples is due to calcination residual carbon and organic volatilization from precursors.

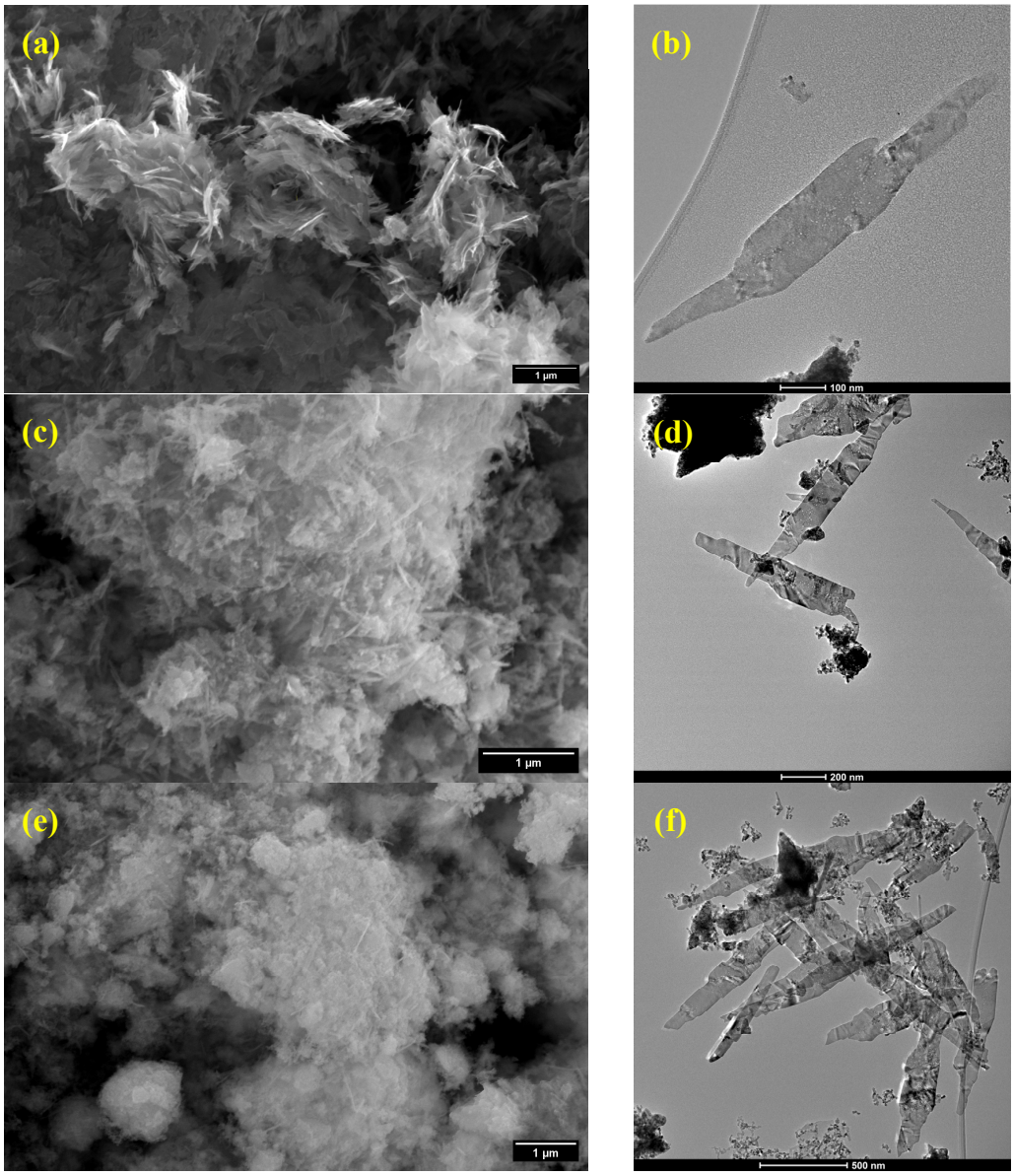

Figure 3. *Cont.*

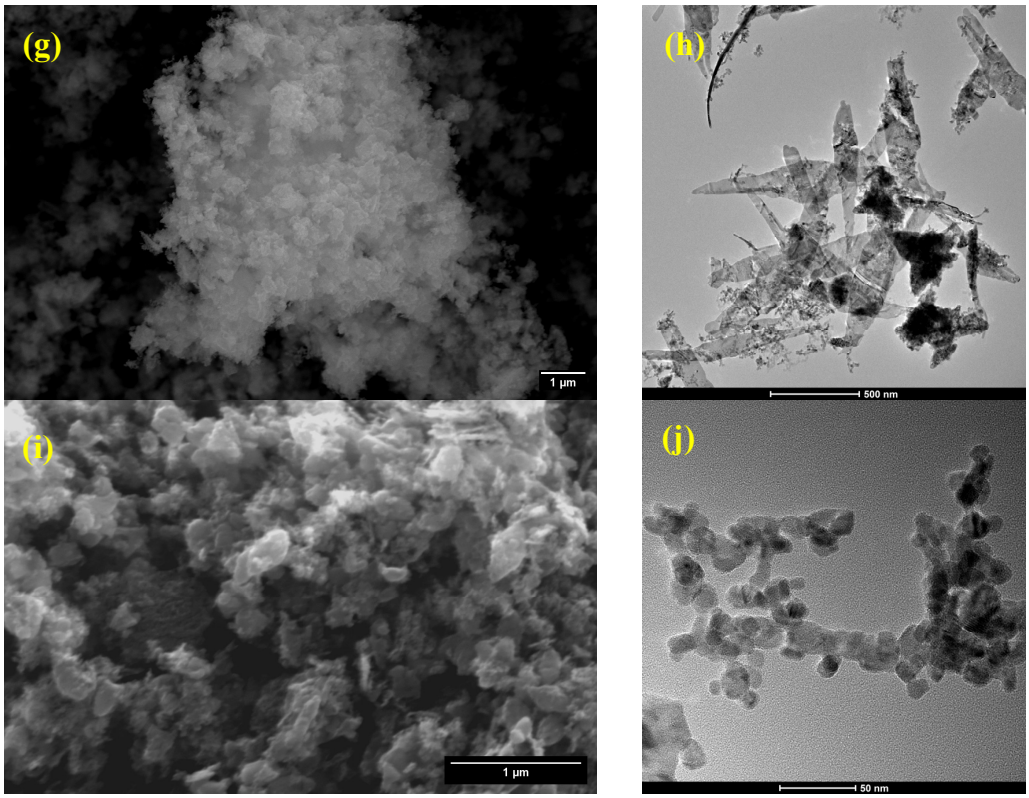

Figure 3. Scanning and Transmission Electron Microscopy images of (**a**,**b**) CuO, (**c**,**d**) ZnO-CuO (25:75), (**e**,**f**) ZnO-CuO (50:50), (**g**,**h**) ZnO-CuO (75:25), and (**i**,**j**) ZnO.

Transmission Electron Microscopy (TEM) images are displayed in Figure 3b,d,f,h,j), and the particle size distribution is displayed in Figure S2. Comparing the average sizes and standard deviations obtained after analyzing several images, the data reveal a clear trend. Pure CuO exhibited 477 ± 275 nm sized leaves, decreasing to 439 ± 260 nm in the ZnO-CuO (25:75) composite as small ZnO nanoparticles began adsorbing onto surfaces. However, the ZnO-CuO (50:50) composite showed considerably larger 702 ± 307 nm particles, implying a large surface for ZnO growth and generating severe aggregation from ZnO bridging between CuO leaves. Thereafter, the 75:25 ratio limited amassing with 487 ± 234 nm sizes. Pure ZnO nanoparticles possessed small 25 ± 7 nm irregular morphologies. Hence, the nanoparticulate decoration of ZnO onto CuO lever and pore surfaces seems to first assist crystalline growth before later inducing aggregation through interlinkage.

Table 2. EDS Elemental Analysis of ZnO-CuO Composite Materials.

Element	Sample				
	ZnO (100)	**ZnO-CuO (25:75)**	**ZnO-CuO (50:50)**	**ZnO-CuO (75:25)**	**CuO (100)**
Zn (Atom %)	30.42	5.85	15.93	19.95	-
Cu (Atom %)	-	20.33	17.00	6.07	27.46
O (Atom %)	19.79	60.24	57.04	59.69	61.32
C (Atom %)	49.79	13.58	10.03	14.29	11.21

3.4. Analysis of Arsenic (III) Adsorption

The arsenic (III) removal efficiency of the synthesized ZnO-CuO nanocomposites was evaluated in batch adsorption trials performed under pH 7 conditions, starting with an initial arsenic concentration of 10 mg/L (Figure 4). Prior to these experiments, meticulous calibration of the atomic absorption spectrometer was conducted, yielding an impressive

R-squared value of 0.999 (Figure S1). Then, three nanocomposite samples with varying ZnO:CuO molar ratios of 25:75, 50:50, and 75:25 were tested. It was observed that arsenic (III) removal efficiency was strongly dependent on the composition, with the ZnO-CuO (50:50) nanocomposite demonstrating a maximum removal of 70.5%. The ZnO-CuO (25:75) and ZnO-CuO (75:25) composites showed relatively lower removal rates of 43.02% and 63%, respectively. In comparison, pure CuO and ZnO nanoparticles exhibited relatively low removal rates of 1.02% and 0.41%, respectively. The enhanced performance of the 50:50 nanocomposite can be attributed to optimal synergistic effects between ZnO and CuO at this ratio for providing abundant hydroxylated surface binding sites for arsenic (III) adsorption [44,64]. The abundance of these hydroxyl groups facilitated arsenic (III) removal at pH 7 through mechanisms like surface complexation and ion exchange [46,65].

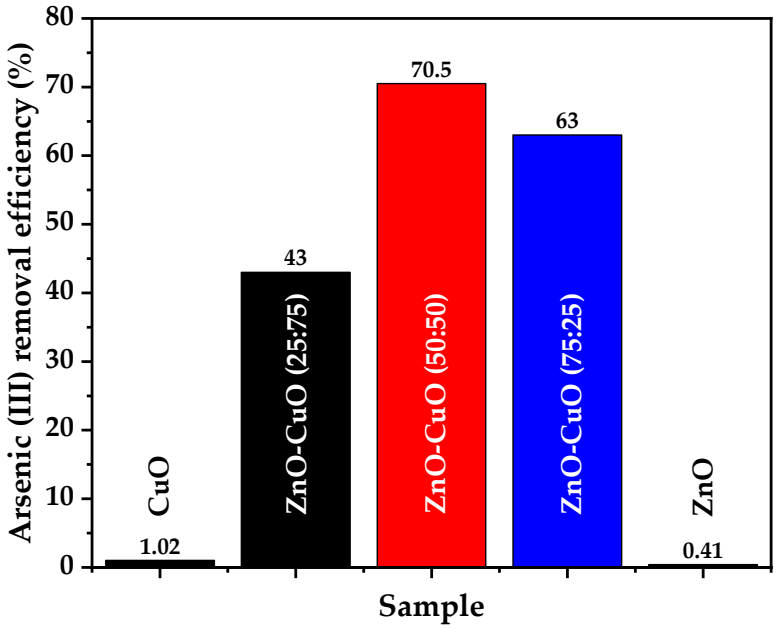

Figure 4. Arsenic removal efficiency of ZnO-CuO nanocomposite.

3.5. pH Influence on Arsenic (III) Removal

The influence of contact time on the arsenic (III) adsorption capacity of the 50:50 ZnO-CuO nanocomposite was evaluated at varying pH levels, as depicted in Figure 5a. It was evident that the amount of arsenic adsorbed rapidly increased during the initial stages of contact between the adsorbate and the adsorbent. This was followed by the attainment of adsorption equilibrium after 120 min for all tested pH conditions. The initial rapid uptake indicates fast diffusion and accessibility of the arsenic species to the binding sites on the nanocomposite surface. The plateau after 120 min signifies saturation of the available adsorption sites. The fast adsorption kinetics are beneficial for potential applications, as they would require shorter residence times.

Batch adsorption experiments revealed a maximum arsenic (III) removal of 85% by the ZnO-CuO (50:50) nanocomposite at pH 5 after 2 h. The abundant hydroxyl groups on the nanocomposite surface, coupled with the positive surface charge under acidic conditions, promoted favorable chemisorption interactions with arsenic (III) species. Speciation studies show that at pH 5, arsenic exists predominantly as neutral H_3AsO_3, which can directly bind to positively charged surface sites via inner-sphere complexation.

The kinetics of arsenic (III) adsorption by the ZnO-CuO nanocomposites under varying pH conditions were analyzed using two common kinetic models—the pseudo-first order and pseudo-second order rate equations [36].

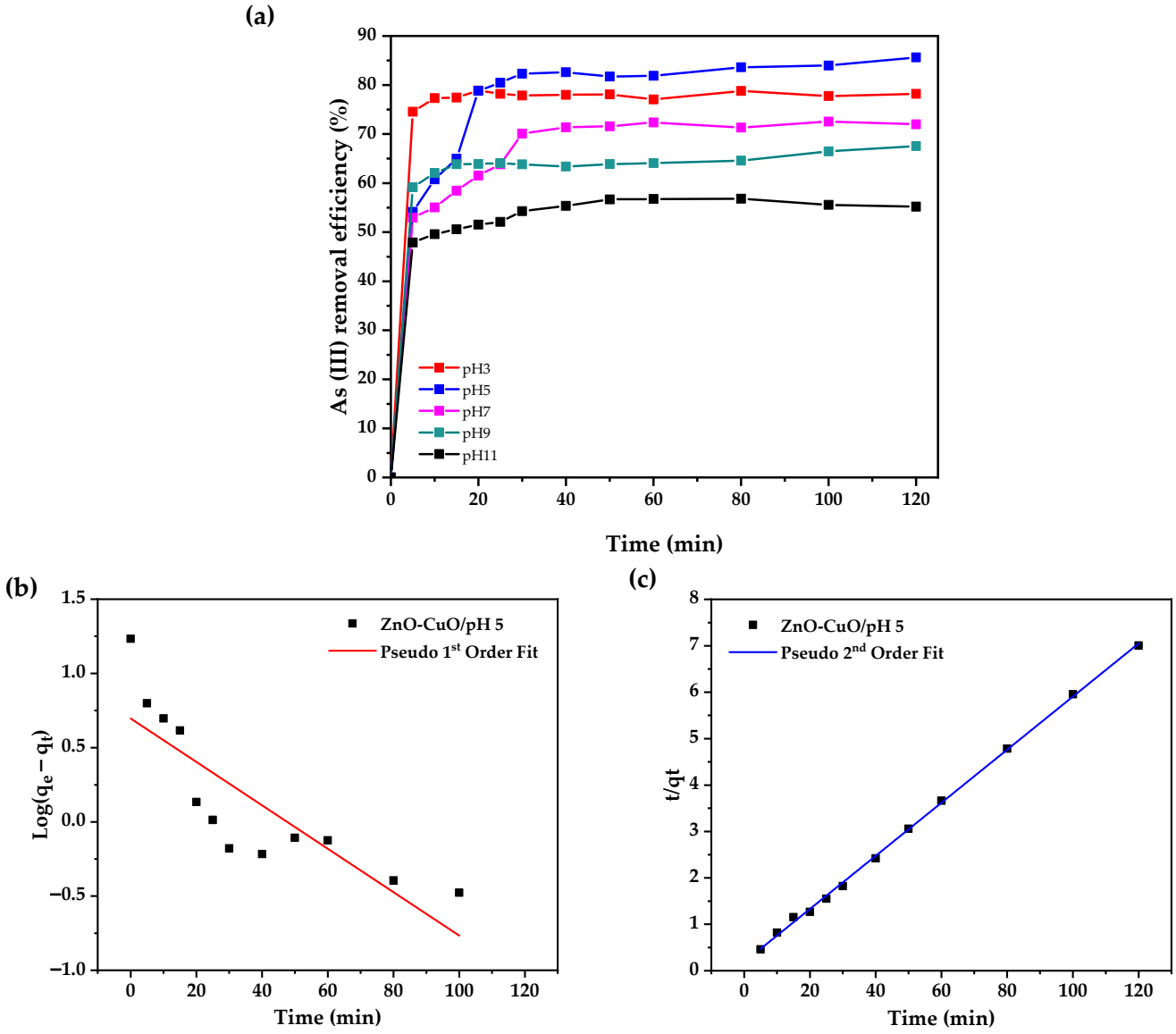

Figure 5. (**a**) Time-dependent arsenic (III) adsorption by ZnO-CuO (50:50) at various pH, with the initial arsenic concentration set at 10 mg/L and adsorbent concentration at 0.5 g/L; (**b**) Linear fitting of the kinetic adsorption utilizing the pseudo-first-order model; and (**c**) Linear fitting using the pseudo-second-order model.

The pseudo-first-order model (Equation (1)) assumes that adsorption occurs through a physisorption mechanism with weak interactions between the adsorbate and the adsorbent surface. The pseudo-second-order model (Equation (2)) assumes that chemisorption is the rate-limiting step involving stronger chemical bonding via the exchange or sharing of electrons between adsorbent and adsorbate [66].

$$\frac{dq_t}{dt} = k_1(q_e - q_t) \quad (1)$$

$$\frac{dq_t}{dt} = k_2(q_e - q_t)^2 \quad (2)$$

where q_t denotes the adsorption capacity at time t; q_e denotes the adsorption capacity at equilibrium, while k_1 and k_2 represent the rate constants for pseudo-first and pseudo-

second-order kinetics, respectively. Equations (3) and (4) provide the linearized forms of these kinetic expressions.

$$log\frac{(q_e - q_t)}{q_e} = -\frac{k_1}{2.303}t \quad (3)$$

$$\frac{t}{q_t} = \frac{1}{k_2 q_e^2} + \frac{t}{q_e} \quad (4)$$

The obtained kinetic coefficients are presented in Table 2.

The results show that the kinetic data fitted both models (Figure 5b,c) and present decent correlation coefficients (R^2), as shown in Table 3, indicating that the arsenite adsorption follows multiple steps [67,68]. However, the pseudo-second-order model demonstrated a better fit overall, with R^2 values very close to 1. According to Ho et al. [67], the excellent fit of the experimental kinetic data to the pseudo-second-order model suggests that chemisorption is likely to be the rate-limiting step controlling the kinetics of arsenic adsorption by the ZnO-CuO nanocomposite.

Table 3. Kinetic coefficients from pseudo-first-order and pseudo-second-order fitting models based on ZnO-CuO nanocomposites experiment data.

pH	Pseudo 1st Order			Pseudo 2nd Order		
	k_1	q_e	R^2	k_2	q_e	R^2
pH 3	0.01369084	1.19	0.60288	0.62686683	15.63	0.99991
pH 5	0.00634824	2.01	0.70912	0.01764271	17.48	0.99918
pH 7	0.02101172	3.36	0.85998	0.02300911	14.88	0.99959
pH 9	0.01300043	2.30	0.54333	0.04975609	13.44	0.99909
pH 11	0.02208858	2.18	0.98732	0.08071776	11.29	0.99925

Chemisorption involves the formation of strong chemical bonds between the adsorbate and adsorbent surface atoms. This typically occurs through the sharing or exchanging of valence electrons, creating coordinated covalent linkages [69].

Analysis of the pseudo-second-order rate constants (k_2) revealed that the k_2 values progressively decreased as the solution pH increased from acidic to alkaline conditions.

The higher k_2 and faster adsorption kinetics under acidic pH can be attributed to the positive surface charge of the nanocomposite and favorable electrostatic interactions with the negatively charged arsenic (III) ions. Under acidic conditions, the hydroxylated ZnO-CuO surface becomes protonated and acquires a net positive charge [43]. This enhances electrostatic attraction between the positively charged surface binding sites and the anionic arsenite species ($H_3AsO_3^-$ /$HAsO_3^{2-}$), accelerating the rate of chemisorption [70,71]. However, as the pH increases, deprotonation of the surface hydroxyl groups occurs, imparting a negative charge to the nanocomposite surface. This electrostatic repulsion between the now negatively charged surface and anionic arsenite ions likely reduces the chemisorption rate [24,72].

Linear forms of Langmuir and Freundlich models were utilized to characterize the equilibrium adsorption data (Table 4).

Table 4. Adsorption isotherms models and their linear forms.

Isotherm Model	Nonlinear Form	Linear Form	Plot	References
Langmuir	$q_e = \frac{Q_L K_L C_e}{1+K_L C_e}$	$\frac{1}{q_e} = \frac{1}{K_L q_{max}}\frac{1}{C_e} + \frac{1}{q_{max}}$	$\frac{1}{q_e}$ vs. $\frac{1}{C_e}$	[73]
Freundlich	$q_e = K_F C_e^{1/n}$	$lnq_e = lnK_f + \frac{1}{n}lnC_e$	lnq_e vs. lnC_e	[74]

The Langmuir equation assumes monolayer coverage with uniform binding sites, allowing the calculation of the maximum uptake capacity (q_{max}). Its linear form permits the determination of the dimensional equilibrium constant K_L, signifying adsorbate-adsorbent

affinity. Conversely, the empirical Freundlich model presumes multilayer sorption across heterogeneous localities of variant affinities. Hence, binding escalates indefinitely with concentration. The heterogeneity factor $1/n$ provides insights into sorption intensity.

By fitting experimental results to these fundamental isotherms and deriving key parameters, including equilibrium concentration *Ce*, quantity bound at equilibrium q_e, and constants that reveal critical binding tendencies, the adsorption mechanism, capacity, and favorability can be effectively elucidated from a theoretical lens to support the empirical observations.

To enhance comprehension of the adsorption process and ascertain the maximal capacity of arsenic (III) removal using ZnO-CuO (50:50) nanocomposite, adsorption isotherm data were acquired under ambient conditions at a temperature of 25 degrees Celsius. The data were subjected to fitting using the linear equations of the Langmuir and Freundlich models, respectively.

The results displayed in Figure 6 and Table 5 show a superior Freundlich model linear regression fit (R^2 = 0.9856) that verifies heterogeneous multilayer binding of arsenic (III) ions onto the variable ZnO-CuO (50:50) nanocomposite surface [74].

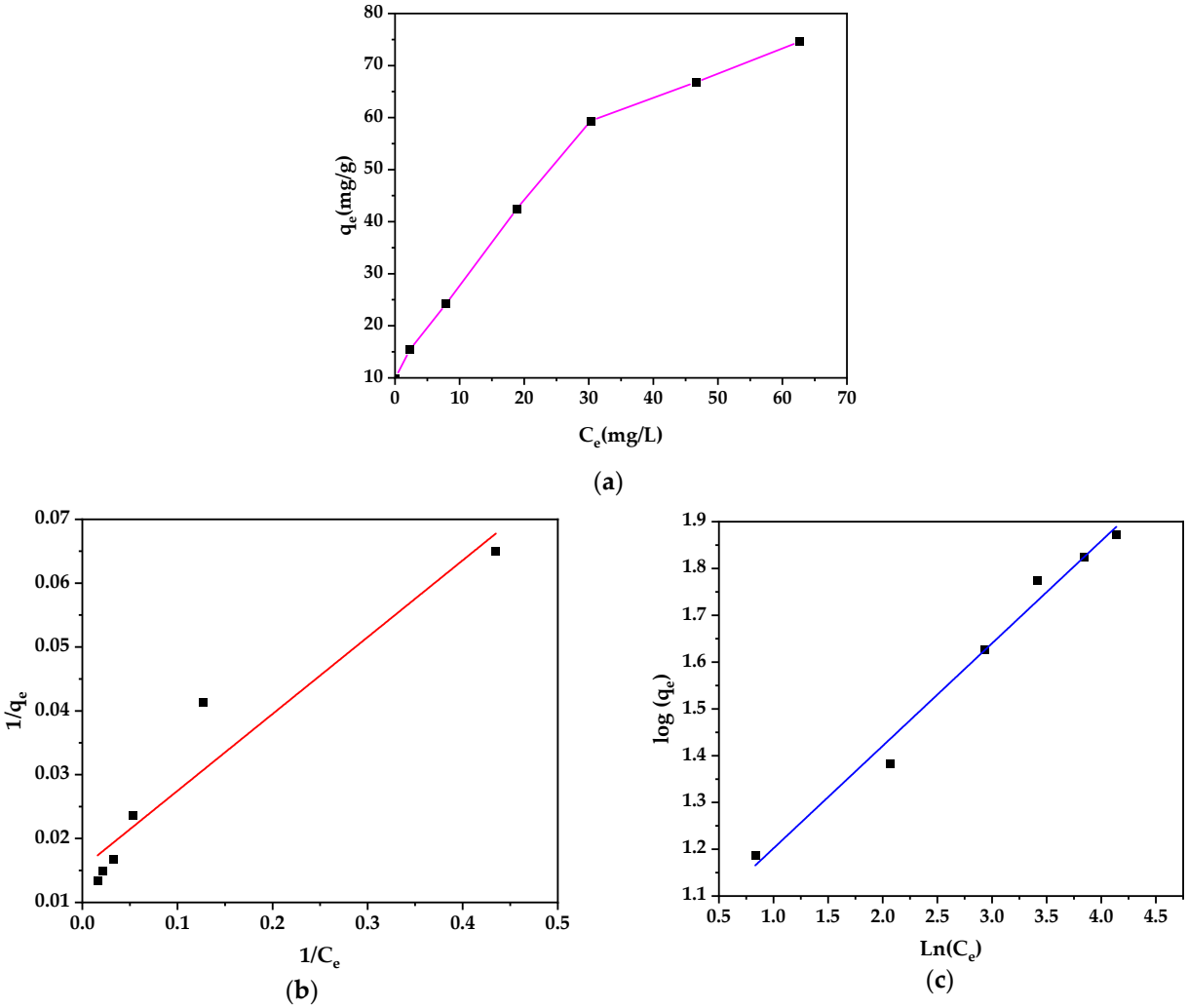

Figure 6. (**a**) Effect of initial concentration of Arsenic (III) removal by ZnO-CuO (50:50) nanocomposite; (**b**) Langmuir's isotherm plot; and (**c**) Freundlich's isotherm plots.

Table 5. Isotherm parameters for the arsenic (III) by ZnO-CuO.

Isotherm Model	**Langmuir**				**Freundlich**		
Parameters	q_{max} **(mg/g)**	K_L	R_L	R^2	K_f	**1/*n***	R^2
Value	64.7668	0.1283	0.4380	0.9243	9.6168	0.2190	0.9856

At acidic pH 5, the neutral H_3AsO_3 species predominates and can access both high- and low-energy binding sites through a combination of inner-sphere direct surface complexation on abundant hydroxyls [75], as well as secondary interactions. This multilayer arrangement leads to a very high overall adsorption capacity [76].

The decent Langmuir fit suggests that while some monolayer coverage occurs at stronger chemisorption sites [77], the diverse surface enables extensive multilayer arsenic (III) adsorption through the spectrum of weaker physisorption sites [78].

The kinetics showed that chemisorption likely limits the initial uptake rate [79]. Thereafter, rapid diffusion and physisorption drive the high equilibrium capacities by allowing neutral H_3AsO_3 to saturate the heterogeneous surface of the nanocomposite [80].

Table 6 illustrates a comparison of several materials based on ZnO and CuO that have been reported for the removal of arsenic (As).

Through direct ultrasound-mediated nanostructuring, our ZnO-CuO (50:50) nanocomposite demonstrates an appreciable 64.77 mg/g arsenic (III) Langmuir adsorption capacity. This surpasses conventionally fabricated precursors, including pure ZnO (5.03 mg/g) [81] and ZnO-GO (8.17 mg/g) composites [82], validating the intrinsic benefits of synergistic nanotexturing. Notably, only tailor-made supports like solution combustion-derived ZnO-CuO/g-C_3N_4 [46] or dopants with citrate-hydrothermally synthesized Pd@ZnO/CuO [83] enable higher capacities near 100 mg/g. However, despite the absence of expensive adjuncts, our facile sonochemical synthesis elicits emergent morphological properties from interfacial Zn/Cu alloying, conferring substantial As(III) coordination strength.

Additionally, employing only non-toxic, cost-effective metal salts lends promise for sustainable, large-scale adoption. This establishes an easily prepared, competitively performing nano-adsorbent via component manipulation. Further stoichiometric modulation could elucidate mechanisms and systematic property enhancements.

Table 6. Comparative Arsenic Adsorption Capacities in ZnO-CuO Nanocomposites and Other Adsorbents.

Material	**Synthesis Method**	**Test Conditions**	q_{max} **(mg/g)**	**Reference**
ZnO-CuO/g-C_3N_4	Solution combustion method	7 mg of adsorbent; 50 mL of 20–150 ppb As (III) solution; 70 min	97.56	[46]
CuO-ZnO	Electrospinning	5 mg of adsorbent; 10 mL of 1–9 ppm As (III) solution; 24 h	26.27	[44]
ZnO-GO	Solvothermal	0.3 g of adsorbent; 100 mL of 10–50 ppm As (III) solution; 1 h.	8.17	[82]
CuO-ZnO doped chitosan succinic acid	Freeze-drying process	10 mg of adsorbent; 5 mL of 0.1–1.2 ppm As (III) solution; 24 h.	0.899	[84]
ZnO	Precipitation	10 mg of adsorbent; 4 mL of 3–1000 ppm As (III) solution	5.03	[81]
ZnO nanorods	Precipitation	0.4 g of adsorbent; 50 mL of 30–90 ppb As (III) solution	38.46	[85]
Pd@ZnO/CuO	Citrate-hydrothermal	10 mg of adsorbent; 10 mL of 250 ppb arsenic solution; 3 h	91.96	[83]
CuO/ZnO	Ultrasound	50 mg of adsorbent; 100 mL of arsenic solution with 10–100 ppm; 2 h	64.77	present work

3.6. PZC Analysis of ZnO-CuO Nanocomposite

The point of zero charge results are displayed in Figure 7. In contrast with the previous results, the maximum 85.63% arsenic (III) removal observed at pH 5 aligns closely with the point of zero charge (PZC) of 6.45 when the net surface charge is minimized, enabling favorable chemisorption [41]. Below the PZC, the positively charged surface attracted anionics H_2AsO^{3-}/$HAsO_3^{2-}$ through electrostatics, conferring 78.18% (pH 3) to 85.63% (pH 5) uptake. Above the PZC, surface repulsion of these species reduced capacity to 72.55% (pH 7), 67.55% (pH 9), and 55.57% (pH 11) as hydroxylated areas grew [86].

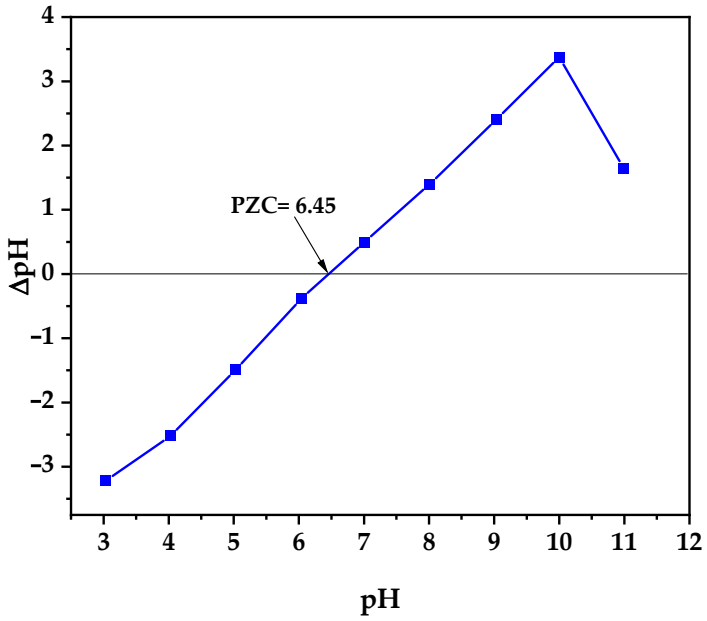

Figure 7. PZC plot for ZnO-CuO nanocomposite by salt addition method.

Explicitly integrating adsorption capacities across the pH range with PZC-governed surface charging provides in-depth insights into the multifaceted electrostatic and chemical factors influencing nano-adsorption [87]. The direct relationship of solution chemistry with binding verifies the intricate interplay of site competition, surface speciation, and charge repulsion in directing pH-responsive arsenic (III) removal.

3.7. Impact of Coexisting Ions

The adsorption of arsenic (III) by ZnO-CuO (50:50) nanocomposites at pH 7 occurs primarily through surface complexation mechanisms involving inner-sphere and outer-sphere binding to surface metal ions and hydroxyl groups [88,89]. The presence of competing anions can interfere with arsenic (III) adsorption by occupying these chemisorption sites or altering surface charge. As seen in Figure 8, increasing concentrations of chloride, nitrate, and sulfate ions (100 to 500 mg/L) at pH 7 all progressively reduced arsenic (III) removal efficiency by the nanocomposite. At the highest concentration (500 mg/L), chloride lowered removal from 72.9% to 47%, nitrate to 47.8%, and sulfate to 49.5%. The monovalent chloride ion likely competes directly with arsenite oxyanions for surface binding [83]. The multivalent sulfate and nitrate ions have greater hydration energies, displacing arsenic (III) through the outer-sphere complex formation [90,91]. Also, specific adsorption of sulfate and nitrate imparted a more negative surface charge at pH 7, weakening the arsenic (III) electrostatic attraction [92].

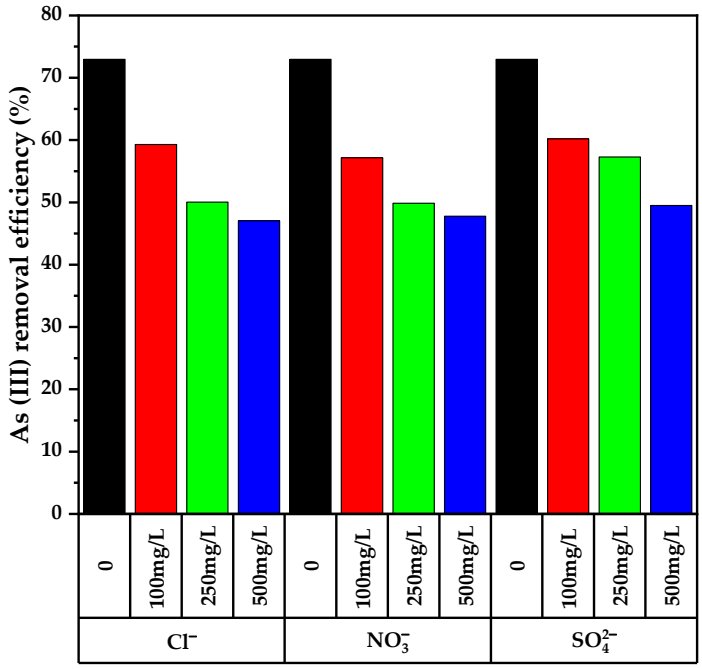

Figure 8. Influence of different competing ions on arsenic (III) removal using ZnO-CuO (50:50).

Despite current experimental limitations for statistical testing, the substantial arsenic adsorption capacity of the synthesized ZnO-CuO nanocomposite through sonochemical methods is evident in this evaluation.

3.8. Stability

The effectiveness of the ZnO-CuO (50:50) composite in removing arsenic (III) was the primary topic of an in-depth study that was conducted on the phase stability of the material under varied pH conditions. For the purpose of determining the structural stability of the composite material, an XRD study was carried out. The XRD patterns that were obtained by exposing the ZnO-CuO (50:50) composite to various pH conditions are displayed in Figure 9.

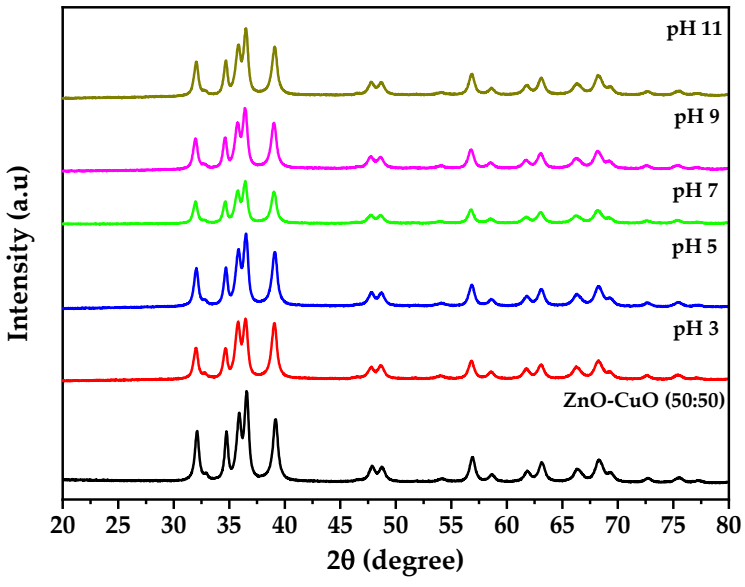

Figure 9. XRD patterns of ZnO-CuO (50:50) after different pH evaluations.

XRD results show that the ZnO-CuO (50:50) composite keeps its original structure across the whole pH range that was tested. The absence of any new phases and the absence of a significant decrease in the abundance of any phase served as evidence that the composite material has chemical stability under varied pH conditions.

The evaluation of arsenic (III) removal uncovered intriguing trends related to pH, which is important to note. At a pH of 5, the ZnO-CuO (50:50) composite showed the best arsenic removal effectiveness, whereas at a pH of 11, the composite showed the lowest removal efficiency. These findings are consistent with the XRD patterns that were found, providing more evidence that phase stability is directly related to arsenic removal efficiency.

4. Conclusions

The ultrasound-assisted coprecipitation method successfully produced optimized ZnO-CuO nanocomposites with a 50:50 molar ratio, demonstrating excellent 85.63% arsenic (III) elimination capacity under acidic conditions (pH 5) where chemisorptive binding with neutral H_3AsO_3 prevailed. Favorable pseudo-second order adsorption kinetics revealed rapid uptake, reaching equilibrium within 2 h. The nanomaterial maintained stability across a broad pH spectrum, retaining selectivity despite competing ions.

Multilayer Freundlich model dominance verified specialized heterogeneous surface textures that enable extensive physisorption-driven stacking, complementing chemisorption. The 64.77 mg/g maximum binding capacity, accessible ultrasonication synthesis, and intrinsic synergies upon nanoscale mixing of Zn/Cu oxides substantiate the promise for sustainable large-scale adoption to mitigate critical arsenic contamination issues.

Moreover, competing ions had a few significant effects on the arsenic adsorption by the ZnO-CuO (50:50) composite. Similarly, the stability of the composite was investigated, revealing that the ZnO-CuO (50:50) nanocomposite maintains its structure over a broad pH range. Thus, such a ZnO-CuO composite has true potential as a nanocomposite for water remediation applications.

Supplementary Materials: The following supporting information can be downloaded at: https://www.mdpi.com/article/10.3390/w15244318/s1, Figure S1. Graphite furnace Atomic absorption spectrometer calibration curve of arsenic (III). Figure S2. Particle size distribution of pure ZnO, CuO and ZnO-CuO nanocomposite.

Author Contributions: J.P.M.S. and F.G.G., funding acquisition, experiment design, investigation, and review and editing; E.J.S.S., experiment design, investigation, characterization, data analysis, and writing—original draft, review, and editing; W.O.L.R., investigation and characterization; R.M.T.C., E.M.F., V.Y.P. and W.D.F.P.d.L. performed data analysis and writing—original draft; E.M.L.S., investigation and characterization. All authors have read and agreed to the published version of the manuscript.

Funding: This research was funded by the Universidad Nacional Jorge Basadre Grohmann through "Fondos del canon sobrecanon y regalias mineras", approved by rectoral resolution N° 3780-2014-UN/JBG with the project "Study of the application of nanotechnology for the purification of water with arsenic in the Tacna region".

Data Availability Statement: The data presented in this study are available on request from the corresponding author.

Acknowledgments: We are grateful to the Universidad Nacional Jorge Basadre Grohmann and the projects "Development of thin films of MWCNT/TiO_2 to improve the efficiency of dye-sensitized solar cells (DSSC)" and "Determination of the optical fingerprints of solid, liquid and organic materials using visible and infrared spectroscopy", of the Universidad Nacional Jorge Basadre Grohmann, approved by rectoral resolutions No. 4516-2018-UN/JBG and No. 5854-2019-UN/JBG, respectively, for their facilities for materials characterization.

Conflicts of Interest: The authors declare no conflict of interest.

References

1. Sankhla, M.S.; Kumari, M.; Nandan, M.; Kumar, R.; Agrawal, P. Heavy Metals Contamination in Water and Their Hazardous Effect on Human Health—A Review. *Int. J. Curr. Microbiol. App. Sci.* **2016**, *5*, 759–766. [CrossRef]
2. Vareda, J.P.; Valente, A.J.M.; Durães, L. Assessment of heavy metal pollution from anthropogenic activities and remediation strategies: A review. *J. Environ. Manag.* **2019**, *246*, 101–118. [CrossRef]
3. Tchounwou, P.B.; Yedjou, C.G.; Patlolla, A.K.; Sutton, D.J. Heavy metal toxicity and the environment. *Exp. Suppl.* **2012**, *101*, 133–164. [CrossRef] [PubMed]
4. Garelick, H.; Jones, H.; Dybowska, A.; Valsami-Jones, E. Arsenic pollution sources. *Rev. Environ. Contam. Toxicol.* **2008**, *197*, 17–60. [CrossRef] [PubMed]
5. Han, F.X.; Su, Y.; Monts, D.L.; Plodinec, M.J.; Banin, A.; Triplett, G.E. Assessment of global industrial-age anthropogenic arsenic contamination. *Naturwissenschaften* **2003**, *90*, 395–401. [CrossRef] [PubMed]
6. Rahman, M.M.; Chowdhury, U.K.; Mukherjee, S.C.; Mondal, B.K.; Paul, K.; Lodh, D.; Biswas, B.K.; Chanda, C.R.; Basu, G.K.; Saha, K.C.; et al. Chronic arsenic toxicity in Bangladesh and West Bengal, India—A review and commentary. *J. Toxicol. Clin. Toxicol.* **2001**, *39*, 683–700. [CrossRef] [PubMed]
7. Chowdhury, U.K.; Biswas, B.K.; Chowdhury, T.R.; Samanta, G.; Mandal, B.K.; Basu, G.C.; Chanda, C.R.; Lodh, D.; Saha, K.C.; Mukherjee, S.K.; et al. Groundwater arsenic contamination in Bangladesh and West Bengal, India. *Environ. Health Perspect.* **2000**, *108*, 393–397. [CrossRef]
8. Litter, M.I.; Ingallinella, A.M.; Olmos, V.; Savio, M.; Difeo, G.; Botto, L.; Farfán Torres, E.M.; Taylor, S.; Frangie, S.; Herkovits, J.; et al. Arsenic in Argentina: Occurrence, human health, legislation and determination. *Sci. Total Environ.* **2019**, *676*, 756–766. [CrossRef]
9. Alam, M.A.; Mukherjee, A.; Bhattacharya, P.; Bundschuh, J. An appraisal of the principal concerns and controlling factors for Arsenic contamination in Chile. *Sci. Rep.* **2023**, *13*, 11168. [CrossRef]
10. Osuna-Martínez, C.C.; Armienta, M.A.; Bergés-Tiznado, M.E.; Páez-Osuna, F. Arsenic in waters, soils, sediments, and biota from Mexico: An environmental review. *Sci. Total Environ.* **2021**, *752*, 142062. [CrossRef]
11. Ramos, W.; Ortega-Loayza, A.G.; Díaz, J.; de La Cruz-Vargas, J.A.; Tello, M.; Ronceros, G.; Loayza, M.; Gutierrez, E.L. Arsenicism by Chronic Exposure to Mine Tailings in Peru: An Analysis of 17 Cases with Lesions on Skin and/or Annexes. *Clin. Cosmet. Investig. Dermatol.* **2022**, *15*, 2407–2414. [CrossRef] [PubMed]
12. Custodio, M.; Cuadrado, W.; Peñaloza, R.; Montalvo, R.; Ochoa, S.; Quispe, J. Human Risk from Exposure to Heavy Metals and Arsenic in Water from Rivers with Mining Influence in the Central Andes of Peru. *Water* **2020**, *12*, 1946. [CrossRef]
13. Custodio, M.; Peñaloza, R. Evaluation of the Distribution of Heavy Metals and Arsenic in Inland Wetlands (Peru) Using Multivariate Statistical Methods. *Ecol. Eng. Environ. Technol.* **2021**, *22*, 104–111. [CrossRef]
14. Mamani Lopez, E.P.; Chambilla Quispe, V. Análisis Fisicoquímico Y Biológico Del Agua Para Consumo Humano En El Distrito De Huanuara. *Cienc. Desarro.* **2019**, *11*, 67–70. [CrossRef]
15. World Health Organization. *Arsenic in Drinking-Water: Background Document for Development of WHO Guidelines for Drinking-Water Quality*; World Health Organization: Geneva, Switzerland, 2019.
16. Abernathy, C.O.; Liu, Y.P.; Longfellow, D.; Aposhian, H.V.; Beck, B.; Fowler, B.; Goyer, R.; Menzer, R.; Rossman, T.; Thompson, C.; et al. Arsenic: Health effects, mechanisms of actions, and research issues. *Environ. Health Perspect.* **1999**, *107*, 593–597. [CrossRef]
17. Chen, Y.; Parvez, F.; Gamble, M.; Islam, T.; Ahmed, A.; Argos, M.; Graziano, J.H.; Ahsan, H. Arsenic exposure at low-to-moderate levels and skin lesions, arsenic metabolism, neurological functions, and biomarkers for respiratory and cardiovascular diseases: Review of recent findings from the Health Effects of Arsenic Longitudinal Study (HEALS) in Bangladesh. *Toxicol. Appl. Pharmacol.* **2009**, *239*, 184–192. [CrossRef]
18. McDermott, T.R.; Stolz, J.F.; Oremland, R.S. Arsenic and the gastrointestinal tract microbiome. *Environ. Microbiol. Rep.* **2020**, *12*, 136–159. [CrossRef]
19. Vahidnia, A.; van der Voet, G.B.; de Wolff, F.A. Arsenic neurotoxicity—A review. *Hum. Exp. Toxicol.* **2007**, *26*, 823–832. [CrossRef]
20. Mayer, J.E.; Goldman, R.H. Arsenic and skin cancer in the USA: The current evidence regarding arsenic-contaminated drinking water. *Int. J. Dermatol.* **2016**, *55*, e585–e591. [CrossRef]
21. Vineetha, V.P.; Raghu, K.G. An Overview on Arsenic Trioxide-Induced Cardiotoxicity. *Cardiovasc. Toxicol.* **2019**, *19*, 105–119. [CrossRef]
22. Kile, M.L.; Mazumdar, M. Arsenic and developmental toxicity and reproductive disorders. In *Handbook of Arsenic Toxicology*; Elsevier: Amsterdam, The Netherlands, 2023; pp. 593–605. ISBN 9780323898478.
23. Korte, N.E.; Fernando, Q. A review of arsenic (III) in groundwater. *Crit. Rev. Environ. Control* **1991**, *21*, 1–39. [CrossRef]
24. Bissen, M.; Frimmel, F.H. Arsenic—A Review. Part II: Oxidation of Arsenic and its Removal in Water Treatment. *Acta Hydrochim. Hydrobiol.* **2003**, *31*, 97–107. [CrossRef]
25. Kowalski, K.P. Advanced Arsenic Removal Technologies Review. In *Chemistry of Advanced Environmental Purification Processes of Water*; Elsevier: Amsterdam, The Netherlands, 2014; pp. 285–337. ISBN 9780444531780.
26. Ng, K.-S.; Ujang, Z.; Le-Clech, P. Arsenic Removal Technologies for Drinking Water Treatment. *Re/Views Environ. Sci. Bio/Technol.* **2004**, *3*, 43–53. [CrossRef]
27. Carneiro, M.A.; Pintor, A.M.A.; Boaventura, R.A.R.; Botelho, C.M.S. Current Trends of Arsenic Adsorption in Continuous Mode: Literature Review and Future Perspectives. *Sustainability* **2021**, *13*, 1186. [CrossRef]

28. Frankenberger, J.W.T. *Environmental Chemistry of Arsenic*; CRC Press: Boca Raton, FL, USA, 2001; ISBN 9780429180071.
29. Mohan, D.; Pittman, C.U. Arsenic removal from water/wastewater using adsorbents—A critical review. *J. Hazard. Mater.* **2007**, *142*, 1–53. [CrossRef] [PubMed]
30. Guan, X.; Du, J.; Meng, X.; Sun, Y.; Sun, B.; Hu, Q. Application of titanium dioxide in arsenic removal from water: A review. *J. Hazard. Mater.* **2012**, *215–216*, 1–16. [CrossRef] [PubMed]
31. Ashraf, S.; Siddiqa, A.; Shahida, S.; Qaisar, S. Titanium-based nanocomposite materials for arsenic removal from water: A review. *Heliyon* **2019**, *5*, e01577. [CrossRef]
32. Gamarra, F.; Medina, J.; Lanchipa, W.; Tamayo, R.; Sacari, E. Structural, Optical, and Arsenic Removal Properties of Sol-Gel Synthesized Fe-Doped TiO_2 Nanoparticles. *Nanomaterials* **2022**, *12*, 3402. [CrossRef]
33. Das, T.K.; Bezbaruah, A.N. Comparative study of arsenic removal by iron-based nanomaterials: Potential candidates for field applications. *Sci. Total Environ.* **2021**, *764*, 142914. [CrossRef]
34. Shan, H.; Mo, H.; Liu, Y.; Zeng, C.; Peng, S.; Zhan, H. As(III) removal by a recyclable granular adsorbent through dopping Fe-Mn binary oxides into graphene oxide chitosan. *Int. J. Biol. Macromol.* **2023**, *237*, 124184. [CrossRef]
35. Opiso, E.M.; Tabelin, C.B.; Ramos, L.M.; Gabiana, L.J.R.; Banda, M.H.T.; Delfinado, J.R.Y.; Orbecido, A.H.; Zoleta, J.B.; Park, I.; Arima, T.; et al. Development of a three-step approach to repurpose nickel-laterite mining waste into magnetite adsorbents for As(III) and As(V) removal: Synthesis, characterization and adsorption studies. *J. Environ. Chem. Eng.* **2023**, *11*, 108992. [CrossRef]
36. Tamayo, R.; Espinoza-González, R.; Gracia, F.; Rodrigues-Filho, U.P.; Flores, M.; Sacari, E. As(III) Removal from Aqueous Solution by Calcium Titanate Nanoparticles Prepared by the Sol Gel Method. *Nanomaterials* **2019**, *9*, 733. [CrossRef]
37. Shanmugaraj, K.; Vinoth, V.; Pugazhenthiran, N.; Valdés, H.; Salvo, C.; Sepúlveda, E.; Viswanathan Mangalaraja, R. Ferrihydrite−Graphene Oxide Foams as an Efficient Adsorbent for Arsenic(III) Removal from an Aqueous Solution. *Inorg. Chem. Commun.* **2023**, *153*, 110892. [CrossRef]
38. Singh, D.K.; Mohan, S.; Kumar, V.; Hasan, S.H. Kinetic, isotherm and thermodynamic studies of adsorption behaviour of CNT/CuO nanocomposite for the removal of As(III) and As(V) from water. *RSC Adv.* **2016**, *6*, 1218–1230. [CrossRef]
39. Siddiqui, S.I.; Naushad, M.; Chaudhry, S.A. Promising prospects of nanomaterials for arsenic water remediation: A comprehensive review. *Process Saf. Environ. Prot.* **2019**, *126*, 60–97. [CrossRef]
40. Massoudinejad, M.; Keramati, H.; Ghaderpoori, M. Investigation of photo-catalytic removal of arsenic from aqueous solutions using UV/H_2O_2 in the presence of ZnO nanoparticles. *Chem. Eng. Commun.* **2020**, *207*, 1605–1615. [CrossRef]
41. Reddy, K.J.; McDonald, K.J.; King, H. A novel arsenic removal process for water using cupric oxide nanoparticles. *J. Colloid Interface Sci.* **2013**, *397*, 96–102. [CrossRef] [PubMed]
42. Samad, A.; Furukawa, M.; Katsumata, H.; Suzuki, T.; Kaneco, S. Photocatalytic oxidation and simultaneous removal of arsenite with CuO/ZnO photocatalyst. *J. Photochem. Photobiol. A Chem.* **2016**, *325*, 97–103. [CrossRef]
43. Vaiano, V.; Iervolino, G.; Rizzo, L. Cu-doped ZnO as efficient photocatalyst for the oxidation of arsenite to arsenate under visible light. *Appl. Catal. B Environ.* **2018**, *238*, 471–479. [CrossRef]
44. Malwal, D.; Gopinath, P. Rapid and efficient removal of arsenic from water using electrospun CuO–ZnO composite nanofibers. *RSC Adv.* **2016**, *6*, 115021–115028. [CrossRef]
45. Savage, N.; Diallo, M.S. Nanomaterials and Water Purification: Opportunities and Challenges. *J. Nanoparticle Res* **2005**, *7*, 331–342. [CrossRef]
46. Khan, Q.U.; Begum, N.; Rehman, Z.U.; Khan, A.U.; Tahir, K.; Tag El Din, E.S.M.; Alothman, A.A.; Habila, M.A.; Liu, D.; Bocchetta, P.; et al. Development of Efficient and Recyclable ZnO-CuO/g-C_3N_4 Nanocomposite for Enhanced Adsorption of Arsenic from Wastewater. *Nanomaterials* **2022**, *12*, 3984. [CrossRef] [PubMed]
47. Penke, Y.K.; Kar, K.K. A review on multi-synergistic transition metal oxide systems towards arsenic treatment: Near molecular analysis of surface-complexation (synchrotron studies/modeling tools). *Adv. Colloid Interface Sci.* **2023**, *314*, 102859. [CrossRef] [PubMed]
48. Lata, S.; Samadder, S.R. Removal of arsenic from water using nano adsorbents and challenges: A review. *J. Environ. Manag.* **2016**, *166*, 387–406. [CrossRef] [PubMed]
49. Khan, Q.U.; Begum, N.; Khan, A.U.; Nazir, S.; Ali, A.; Tahir, K.; Aizaz Ud Din, M.; Afzal, A.M.; Liu, D.; Zhan, Y. Nanocomposite Based Adsorbent for Enhanced Arsenic Removal: Determination of Adsorption Mechanism, Kinetic Study, and Factors Affecting the Adsorption Capability of Nanomaterials. *SSRN J.* **2022**. [CrossRef]
50. Kumar, I.; Ranjan, P.; Quaff, A.R. Cost-effective synthesis and characterization of CuO NPs as a nanosize adsorbent for As (III) remediation in synthetic arsenic-contaminated water. *J. Environ. Health Sci. Eng.* **2020**, *18*, 1131–1140. [CrossRef]
51. Bekru, A.G.; Tufa, L.T.; Zelekew, O.A.; Goddati, M.; Lee, J.; Sabir, F.K. Green Synthesis of a CuO-ZnO Nanocomposite for Efficient Photodegradation of Methylene Blue and Reduction of 4-Nitrophenol. *ACS Omega* **2022**, *7*, 30908–30919. [CrossRef]
52. Mubeen, K.; Irshad, A.; Safeen, A.; Aziz, U.; Safeen, K.; Ghani, T.; Khan, K.; Ali, Z.; ul Haq, I.; Shah, A. Band structure tuning of ZnO/CuO composites for enhanced photocatalytic activity. *J. Saudi Chem. Soc.* **2023**, *27*, 101639. [CrossRef]
53. Renuka, L.; Anantharaju, K.S.; Vidya, Y.S.; Nagaswarupa, H.P.; Prashantha, S.C.; Nagabhushana, H. Synthesis of Sunlight Driven ZnO/CuO Nanocomposite: Characterization, Optical, Electrochemical and Photocatalytic Studies. *Mater. Today Proc.* **2017**, *4*, 11782–11790. [CrossRef]
54. Sakib, A.; Masum, S.; Hoinkis, J.; Islam, R.; Molla, M. Synthesis of CuO/ZnO Nanocomposites and Their Application in Photodegradation of Toxic Textile Dye. *J. Compos. Sci.* **2019**, *3*, 91. [CrossRef]

55. Gholami, P.; Dinpazhoh, L.; Khataee, A.; Orooji, Y. Sonocatalytic activity of biochar-supported ZnO nanorods in degradation of gemifloxacin: Synergy study, effect of parameters and phytotoxicity evaluation. *Ultrason. Sonochem.* **2019**, *55*, 44–56. [CrossRef]
56. Khataee, A.; Kalderis, D.; Gholami, P.; Fazli, A.; Moschogiannaki, M.; Binas, V.; Lykaki, M.; Konsolakis, M. Cu_2O-CuO@biochar composite: Synthesis, characterization and its efficient photocatalytic performance. *Appl. Surf. Sci.* **2019**, *498*, 143846. [CrossRef]
57. Gupta, K.; Joshi, P.; Gusain, R.; Khatri, O.P. Recent advances in adsorptive removal of heavy metal and metalloid ions by metal oxide-based nanomaterials. *Coord. Chem. Rev.* **2021**, *445*, 214100. [CrossRef]
58. Ayub, A.; Raza, Z.A.; Majeed, M.I.; Tariq, M.R.; Irfan, A. Development of sustainable magnetic chitosan biosorbent beads for kinetic remediation of arsenic contaminated water. *Int. J. Biol. Macromol.* **2020**, *163*, 603–617. [CrossRef] [PubMed]
59. Winiarski, J.; Tylus, W.; Winiarska, K.; Szczygieł, I.; Szczygieł, B. XPS and FT-IR Characterization of Selected Synthetic Corrosion Products of Zinc Expected in Neutral Environment Containing Chloride Ions. *J. Spectrosc.* **2018**, *2018*, 2079278. [CrossRef]
60. Da Silva-Neto, M.L.; de Oliveira, M.C.A.; Dominguez, C.T.; Lins, R.E.M.; Rakov, N.; de Araújo, C.B.; Menezes, L.d.S.; de Oliveira, H.P.; Gomes, A.S.L. UV random laser emission from flexible ZnO-Ag-enriched electrospun cellulose acetate fiber matrix. *Sci. Rep.* **2019**, *9*, 11765. [CrossRef]
61. Srivastava, R.; Anu Prathap, M.U.; Kore, R. Morphologically controlled synthesis of copper oxides and their catalytic applications in the synthesis of propargylamine and oxidative degradation of methylene blue. *Colloids Surf. A Physicochem. Eng. Asp.* **2011**, *392*, 271–282. [CrossRef]
62. Ramimoghadam, D.; Hussein, M.Z.B.; Taufiq-Yap, Y.H. Synthesis and characterization of ZnO nanostructures using palm olein as biotemplate. *Chem. Cent. J.* **2013**, *7*, 71. [CrossRef]
63. Phoohinkong, W.; Foophow, T.; Pecharapa, W. Synthesis and characterization of copper zinc oxide nanoparticles obtained via metathesis process. *Adv. Nat. Sci. Nanosci. Nanotechnol.* **2017**, *8*, 35003. [CrossRef]
64. Dhiman, V.; Kondal, N. ZnO Nanoadsorbents: A potent material for removal of heavy metal ions from wastewater. *Colloid Interface Sci. Commun.* **2021**, *41*, 100380. [CrossRef]
65. Hou, S.; Ding, W.; Liu, S.; Zheng, H.; Zhai, J.; Yang, L.; Zhong, Z. Fast oxidation and deep removal of As(III) by integrating metal–organic framework ZIF-67 and sulfite: Performance and mechanism. *Chem. Eng. J.* **2023**, *460*, 141785. [CrossRef]
66. Moussout, H.; Ahlafi, H.; Aazza, M.; Maghat, H. Critical of linear and nonlinear equations of pseudo-first order and pseudo-second order kinetic models. *Karbala Int. J. Mod. Sci.* **2018**, *4*, 244–254. [CrossRef]
67. Ho, Y.-S. Review of second-order models for adsorption systems. *J. Hazard. Mater.* **2006**, *136*, 681–689. [CrossRef] [PubMed]
68. Plazinski, W.; Rudzinski, W.; Plazinska, A. Theoretical models of sorption kinetics including a surface reaction mechanism: A review. *Adv. Colloid Interface Sci.* **2009**, *152*, 2–13. [CrossRef] [PubMed]
69. Ho, Y.; McKay, G. Pseudo-second order model for sorption processes. *Process Biochem.* **1999**, *34*, 451–465. [CrossRef]
70. Verma, L.; Singh, J. Arsenic adsorption from aqueous solution and groundwater using monometallic (Fe) and bimetallic (Fe/Mn) Tectona biochar synthesized from plant refuse: Mechanism, isotherm, and kinetic study. *Environ. Eng. Res.* **2023**, *28*, 220110. [CrossRef]
71. Banerjee, S.; Sharma, Y.C. Synthesis and application of Zn/Ce bimetallic oxides for the decontamination of arsenite (As-III) ions from aqueous solutions. *J. Environ. Manag.* **2019**, *233*, 151–164. [CrossRef] [PubMed]
72. Gao, X.; Root, R.A.; Farrell, J.; Ela, W.; Chorover, J. Effect of silicic acid on arsenate and arsenite retention mechanisms on 6-L ferrihydrite: A spectroscopic and batch adsorption approach. *Appl. Geochem.* **2013**, *38*, 110–120. [CrossRef]
73. Pratt, A. Environmental Applications of Magnetic Nanoparticles. In *Nanomagnetism: Fundamentals and Applications*; Elsevier: Amsterdam, The Netherlands, 2014; pp. 259–307. ISBN 9780080983530.
74. Brdar, M.; Takaci, A.; Sciban, M.; Rakic, D. Isotherms for the adsorption of Cu(II) onto lignin: Comparison of linear and non-linear methods. *Hem. Ind.* **2012**, *66*, 497–503. [CrossRef]
75. Manning, B.A.; Goldberg, S. Adsorption and Stability of Arsenic(III) at the Clay Mineral−Water Interface. *Environ. Sci. Technol.* **1997**, *31*, 2005–2011. [CrossRef]
76. Xie, M.; Luo, X.; Liu, C.; You, S.; Rad, S.; He, H.; Huang, Y.; Tu, Z. Enhancing mechanism of arsenic(III) adsorption by MnO2-loaded calcined MgFe layered double hydroxide. *RSC Adv.* **2022**, *12*, 25833–25843. [CrossRef] [PubMed]
77. Alam, M.A.; Shaikh, W.A.; Alam, M.O.; Bhattacharya, T.; Chakraborty, S.; Show, B.; Saha, I. Adsorption of As (III) and As (V) from aqueous solution by modified *Cassia fistula* (golden shower) biochar. *Appl. Water Sci.* **2018**, *8*, 198. [CrossRef]
78. Cai, G.; Tian, Y.; Li, L.; Zhang, W.; Huang, R.; Zhang, J.; Wang, Q.; Xu, H.; Zhang, Y. Sulfite activation of Fe-Mn bimetallic oxides for rapid oxidative removal of As(III) in water: Involvement of active Mn(III). *Chem. Eng. J.* **2024**, *479*, 147539. [CrossRef]
79. Yang, Y.; Zhang, R.; Chen, S.; Zhu, J.; Wu, P.; Huang, J.; Qi, S. Arsenic(iii) removal from aqueous solution using TiO_2-loaded biochar prepared by waste Chinese traditional medicine dregs. *RSC Adv.* **2022**, *12*, 7720–7734. [CrossRef] [PubMed]
80. Navarathna, C.M.; Karunanayake, A.G.; Gunatilake, S.R.; Pittman, C.U.; Perez, F.; Mohan, D.; Mlsna, T. Removal of Arsenic(III) from water using magnetite precipitated onto Douglas fir biochar. *J. Environ. Manag.* **2019**, *250*, 109429. [CrossRef] [PubMed]
81. Morales, H.M.; Torreblanca, G.; Mar, A.; Alcoutlabi, M.; Eubanks, T.M.; Plata, E.; Parsons, J.G. Investigation of the Thermodynamics for the Removal of As(III) and As(V) from Water Using Synthesized ZnO Nanoparticles and the Effects of pH, Temperature, and Time. *Appl. Sci.* **2023**, *13*, 10525. [CrossRef]
82. Singh, S.; Khasnabis, S.; Anil, A.G.; Kumar, V.; Kumar Naik, T.S.; Nath, B.; Garg, V.K.; Singh, J.; Ramamurthy, P.C. Multifunctional nanohybrid for simultaneous detection and removal of Arsenic(III) from aqueous solutions. *Chemosphere* **2022**, *289*, 133101. [CrossRef]

83. Khan, A.U.; Tahir, K.; Khan, Q.U.; Albalawi, K.; Jevtovic, V.; Almarhoon, Z.M.; El-Zahhar, A.A.; Al-Shehri, H.S.; Ullah, S.; Khan, M.U. Scaled-up development of recyclable Pd@ZnO/CuO nanostructure for efficient removal of arsenic from wastewater. *J. Mol. Struct.* **2022**, *1260*, 132828. [CrossRef]
84. Purohit, S.; Chini, M.K.; Chakraborty, T.; Yadav, K.L.; Satapathi, S. Rapid removal of arsenic from water using metal oxide doped recyclable cross-linked chitosan cryogel. *SN Appl. Sci.* **2020**, *2*, 768. [CrossRef]
85. Yuvaraja, G.; Prasad, C.; Vijaya, Y.; Subbaiah, M.V. Application of ZnO nanorods as an adsorbent material for the removal of As(III) from aqueous solution: Kinetics, isotherms and thermodynamic studies. *Int. J. Ind. Chem.* **2018**, *9*, 17–25. [CrossRef]
86. Qiu, Z.; He, X.; Qiu, F.; Yang, D.; Yao, G.; Zhang, T. Efficient oxidation and absorption of As(III) from aqueous solutions for environmental remediation via CuO@MNW membranes. *Sep. Purif. Technol.* **2020**, *250*, 117165. [CrossRef]
87. Othmani, A.; Maitlo, H.A.; Hamimed, S. Factors affecting adsorption capabilities of nanoscale materials. In *Adsorption through Advanced Nanoscale Materials*; Elsevier: Amsterdam, The Netherlands, 2023; pp. 47–64. ISBN 9780443184567.
88. Singh, P.; Sarswat, A.; Pittman, C.U.; Mlsna, T.; Mohan, D. Sustainable Low-Concentration Arsenite As(III) Removal in Single and Multicomponent Systems Using Hybrid Iron Oxide-Biochar Nanocomposite Adsorbents-A Mechanistic Study. *ACS Omega* **2020**, *5*, 2575–2593. [CrossRef] [PubMed]
89. Reddad, Z.; Gerente, C.; Andres, Y.; Le Cloirec, P. Adsorption of several metal ions onto a low-cost biosorbent: Kinetic and equilibrium studies. *Environ. Sci. Technol.* **2002**, *36*, 2067–2073. [CrossRef] [PubMed]
90. Kanematsu, M.; Young, T.M.; Fukushi, K.; Green, P.G.; Darby, J.L. Arsenic(III, V) adsorption on a goethite-based adsorbent in the presence of major co-existing ions: Modeling competitive adsorption consistent with spectroscopic and molecular evidence. *Geochim. Cosmochim. Acta* **2013**, *106*, 404–428. [CrossRef]
91. Tuutijärvi, T.; Repo, E.; Vahala, R.; Sillanpää, M.; Chen, G. Effect of Competing Anions on Arsenate Adsorption onto Maghemite Nanoparticles. *Chin. J. Chem. Eng.* **2012**, *20*, 505–514. [CrossRef]
92. Jain, A.; Loeppert, R.H. Effect of Competing Anions on the Adsorption of Arsenate and Arsenite by Ferrihydrite. *J. Environ. Qual.* **2000**, *29*, 1422–1430. [CrossRef]